JOREK SIMULATION OF INJECTION ASSIMILATION AND RADIATION ASYMMETRY DURING ITER H-MODE DUAL SHATTERED PELLET INJECTIONS

D. Hu¹, F. J. Artola², E. Nardon³, K Munechika², M. Kong⁴, D. Bonfiglio⁵, M. Hoelzl⁶, W. Tang⁶, G.T.A. Huijsmans^{3,7}, Y. Yuan¹, L. Cheng¹, Y. Li¹, and JOREK Team⁸

¹Beihang University, No. 37 Xueyuan Road, Haidian District, 100191 Beijing, China. ²ITER Organization, Route de Vinon sur Verdon, CS 90 046,13067 Saint Paul-lez-Durance, Cedex, France.

³CEA, IRFM, F-13108 Saint-Paul-Lez-Durance, France.

⁴École Polytechnique Fédérale de Lausanne (EPFL), Swiss Plasma Center (SPC), Lausanne, Switzerland.

⁵Consorzio RFX-CNR, ENEA, INFN, Università di Padova, Acciaierie Venete SpA. I-35127 Padova, Italy.

⁶Max Planck Institute for Plasma Physics, Boltzmannstr. 2, 85748 Garching b. M., Germany.
⁷Eindhoven University of Technology, De Rondom 70 5612 AP Eindhoven, the Netherlands.
⁸See the author list of M. Hoelzl et al 2024 Nucl. Fusion 64 112016

Abstract

The disruption mitigation of future high performance tokamaks is a multi-facets problem. For ITER, the Shattered Pellet Injection (SPI) will be used as the primary Disruption Mitigation System (DMS), by which massive amount of hydrogen and neon is introduced to prevent the Thermal Quench (TQ) heat damage, control the Current Quench (CQ) timescale, as well as help with the runaway electron avoidance. To assess the mitigation efficiency, integrated modelling, utilizing the 3D nonlinear MHD code JOREK and synthetic diagnostic tools within the Integrated Modelling & Analysis Suite (IMAS), are carried out to investigate the injection assimilation and the first wall temperature rise asymmetry after dual SPIs into ITER H-mode plasmas. Two kinds of target plasmas are considered, the baseline H-mode and a "degraded H-mode" representing the effect of pre-disruption confinement degradation. It is found that low neon mixture-ratio injection into baseline H-mode tends to result in strong plasmoid drift and accompanied MHD activities as the fragments arrive in the pedestal region, causing premature heat and particle expulsion, which is counter-productive to the disruption mitigation. Increasing the neon mixture ratio and considering the pre-disruption H-L back transition mitigate such behaviour significantly, enhancing the injection assimilation and radiated energy fraction. The maximum first wall temperature rise is found to be well below the tungsten melting threshold for all cases considered, while for some cases it surpasses the Stainless Steel (SS) melting limit. Past experiments suggest such SS melting would only result in surface roughening without significant mass loss, hence such melting is acceptable. Overall, the above reassuring results serve as part of the ongoing ITER DMS specification validation effort, and further investigations with more realistic considerations, such as the fragment rocket effect, will be performed in the near future.

1. INTRODUCTION

One of the main purposes of the ITER Shattered Pellet Injection (SPI) system [1], is the mitigation of thermal loads during the Thermal Quench (TQ) phase of ITER disruptions. The SPI system achieves this by injecting neon-doped (Ne-doped) hydrogen (H) pellet fragments into the plasma. The impurities released from fragment ablation would then cool the plasma down via line radiation and simple dilution effect, resulting in a more uniform energy deposition onto the plasma-facing-components (PFCs) as compared to the conduction and convection heat flux during unmitigated TQs. Nevertheless, the localized nature of the SPI plume compared with the machine size can still lead to localized radiating structures, which, combined with the geometric effect, can cause detrimental asymmetric line radiation loads on the PFCs. It is therefore crucial to assess the simultaneous thermal and line radiation loads mitigation at ITER, as well as to explore injection schemes that optimize material assimilation and favorable TQ conditions for runaway electron avoidance.

Intensive studies, both experimentally [2–6] and numerically [7–10], have been carried out on the total radiated energy and the radiation power density within the plasma volume after SPIs. Despite the invaluable insight provided by the aforementioned studies, the ultimate criterion of the disruption mitigation efficiency should be the heat flux onto the first wall and its accumulated energy impact [11]. While the recent change of the ITER first wall material to tungsten offers more tolerance to such transient heat flux [12], unfavorable radiation heat flux asymmetry is still possible to cause tungsten heat damage, even when the total radiated fraction is favorable.

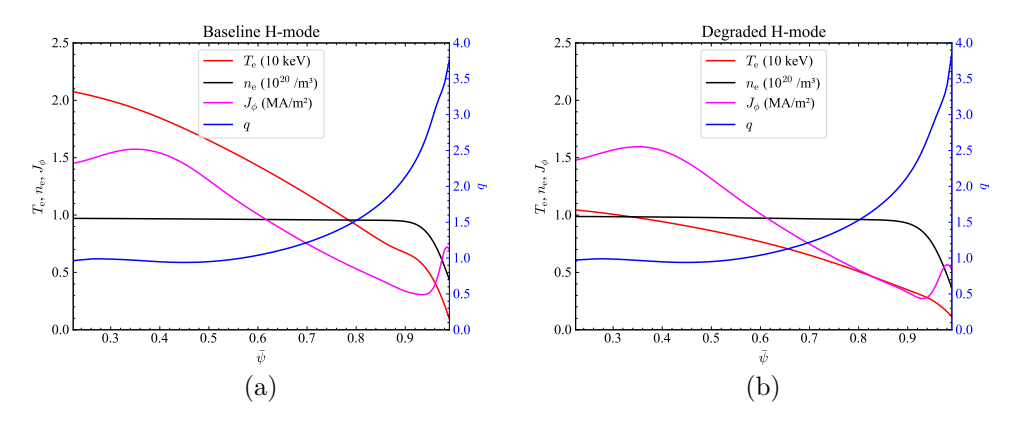


Figure 1 – The initial equilibria of (a) the baseline H-mode and (b) the degraded H-mode, $\bar{\psi}$ is the normalized poloidal flux.

Furthermore, the stainless steel (SS) energy impact threshold is significantly lower than that of tungsten, putting the covers of the port windows at risk of melting, although such melting is acceptable as long as the melt threshold is not dramatically exceeded [13, 14]. Even without exceeding the tolerable maximum energy impact, transient heat fluxes could already produce structural modification on tungsten surface which could affect the mechanical and thermal properties of the first wall [15–19]. Hence it is desirable to obtain the heat flux and energy impact distribution onto the first wall after SPIs to assess the efficiency of the TQ mitigation and to validate the ITER PFC heat tolerance specifications.

Recent JOREK [20, 21] simulations with collisional-radiative impurity model [22] have shown that, for a "degraded H-mode" where the pre-TQ confinement degradation is considered, the ITER dual SPI design is capable of radiating away most of the pre-TQ thermal energy while keeping the maximum wall temperature rise below the tungsten melting threshold, although some acceptable melting is expected for the SS plates [23]. This manuscript incorporates the aformentioned published results and expands upon them to include more scenarios such as the 120 degrees injection case, the finely shattered scenario and the staggered injection scenario. Despite the new scenarios, the conclusion remains the same that the current ITER dual SPI design is capable of handling the radiation asymmetry during the TQ mitigation.

The rest of the manucript is arranged as the follows. The simulation set up is introduced in Section 2. The injection assimilation and radiation asymmetry onto the first wall for both the baseline and degraded H-mode cases are shown in Section 3, and their implication to the PFC damage is discussed. Finally, conclusion and further discussions on the TQ mitigation efficiency with neon SPIs are presented in Section 4.

2. SIMULATION SETUP

Two kinds of target equilibria and two calibers of pellets are considered in this study. One equilibrium is the ITER baseline H-mode equilibrium [24], while the other is a "degraded H-mode" considering the H-L back transition as a result of precursor confinement degradation before the TQ onset [25]. Both cases have the same toroidal magnetic field at $B_T = 5.3T$ and the total plasma current at $I_p = 15MA$. The initial equilibrium profiles, including the electron temperature, density, current density and the safety factor q profiles for both target plasmas are shown in Fig. 1. The initial thermal energy is 190MJ for the degraded H-mode case and 370MJ for the baseline H-mode case.

The SPIs are carried out from the outer equatorial ports EQ-08 and EQ-17, which locate at R=8.4m, Z=0.685m and opposite toroidal positions, along the major radial direction. The vertex angle of the injection cone is 20 degrees. The fragment size distribution follows that of the Statistical Fragmentation model [26, 27]. Our two sets of SPI parameters are the "1% neon full pellet SPI" dual-SPIs with 2.5×10^{22} neon atoms and 1.8×10^{24} hydrogen atoms for each injector, as well as the "5% neon quarter pellet SPI" dual-SPIs with 2.5×10^{22} neon atoms and 4.5×10^{23} hydrogen atoms for each injector. For the full pellet case, the pellet is shattered into 300 fragments, while for the quarter pellet case the fragment number is 100. Their characteristic fragment size is $\kappa_p^{-1} \simeq 1.43mm$ and $\kappa_p^{-1} \simeq 1.30mm$ respectively. Both cases use 500m/s reference injection velocity with $\pm 40\%$ velocity spread. We assume the fragment velocity distributes uniformly over the spreading range, although in reality the velocity distribution has a correlation with the fragment size [28]. We do not expect this to strongly alter the dynamics we investigate here.

We have summarized the cases we investigate in this manuscript in Table 1, where the target equilibria, the neon and hydrogen injection amount, the fragment number and the delay between the injectors are shown. For

Notation	Equilibria	Neon	Hydrogen	Frag.	Delay	$\Delta \phi_{inj}$
BH-FP-dt0 (case 1)	baseline	$2 \times 2.5 \times 10^{22}$	$2 \times 1.8 \times 10^{24}$	300	$0ms^*$	180°
DH-FP-dt0 (case 2)	degraded	$2 \times 2.5 \times 10^{22}$	$2 \times 1.8 \times 10^{24}$	300	0ms	180°
DH-QP-dt0 (case 3)	degraded	$2 \times 2.5 \times 10^{22}$	$2 \times 4.5 \times 10^{23}$	100	0ms	180°
DH-QP-dt1 (case 4)	degraded	$2 \times 2.5 \times 10^{22}$	$2 \times 4.5 \times 10^{23}$	100	1ms	180°
DH-QP-dt0-ff (case 5)	degraded	$2 \times 2.5 \times 10^{22}$	$2 \times 4.5 \times 10^{23}$	1000	0ms	180°
DH-QP-dt0-120 (case 6)	degraded	$2 \times 2.5 \times 10^{22}$	$2 \times 4.5 \times 10^{23}$	100	0ms	120°
DH-QP-stg (case 7)	degraded	2×0	$2 \times 5 \times 10^{23}$	100	0ms	180°
		$+2 \times 2.5 \times 10^{22}$	$+2 \times 4.5 \times 10^{23}$	100	(Staggered)	

Table 1 – The injection parameters for the SPI considered in this study. *Note that for BH-FP-dt0 there exists an asymmetry between the plumes although they are injected at the same time.

all cases, the first fragment of the EQ-08 plume arrives on the LCFS approximately at t=0.38ms and the last one arrives approximately at 0.89ms. All the fragments from the EQ-17 plume in the BH-FP-dt0 case arrive approximately at t=0.54ms since there is no velocity spread by mistakes in the simulation setup. The arrival time of the fragments from the EQ-17 plume for the rest of the cases is the same with that of the EQ-08 plume, plus the delay between the injectors shown in Table 1.

The Integrated Modelling & Analysis Suite (IMAS) integrated RaySect/CHERAB code suite [29, 30] is used to obtain the wall heat flux via ray-tracing the radiation power density obtained by JOREK onto the realistic ITER first wall tiles and the SS armour plate of the diagnostic port windows. Once the heat flux distribution is obtained, the accumulated energy impact is calculated by considering the convolution of the time dependent heat flux $q_s(t)$ [23]:

$$\Delta Q(t) = \frac{1}{2} \int_{t_0}^t \frac{q_s(t')}{\sqrt{t - t'}} dt'. \tag{1}$$

Here t_0 is the beginning time of the heat pulse. The energy impact is then directly linked to the material surface temperature rise [11]:

$$\Delta T(\Delta t) = \frac{2}{\sqrt{\pi b}} \Delta Q(\Delta t). \tag{2}$$

Here $b = \sqrt{\kappa \rho c}$, ρ is the material density, c is its specific heat capacity, κ is its heat conductivity. With a given energy impact, one could checkout the corresponding melting limit for a given material to assess the severity of the heat damage.

3. INJECTION ASSIMILATION AND RADIATION ASYMMETRY

The most important results from the above scenarios are summaried in Table 2. The overall assimilated neon, assimilated hydrogen within the LCFS, radiated energy fraction f_{rad} , approximate TQ timescale defined as the timescale of the thermal energy falling from 90% to 20% of the initial thermal energy, as well as the maximum local energy impact for those seven cases are shown. The relatively low assimilation and radiated fraction in the BH-FP-dt0 case are due to the strong plasmoid drift and accompanying MHD activity as the fragments arrive on the pedestal region [23]. Strong edge MHD perturbation accompanies such drift motion, resulting in strong edge stochasticity and pedestal collapse. It should be noted that almost all of the non-radiative thermal energy loss shown in the table for the DH-QP-stg case occurs during the H injection phase, where the preliminary MHD response creates edge stochasticity which leads to premature heat transport.

3.1. The injection assimilation and penetration

As is mentioned above and reported in Ref. [23], strong plasmoid drift occurs as the fragments enter the baseline H-mode pedestal region. This results in strong material expulsion which is reflected in the BH-FP-dt0 row of Table 2. Such drift could be mitigated by considering the precursor confinement degradation and using higher neon mixture-ratio pellet. One such example could be seen in Fig. 2 where the mid-plane electron density profiles of the BH-FP-dt0 and the DH-QP-dt0 case are compared. The LCFS on the low field side approximately locates at R = 8.2m for both cases. In Fig. 2(a), comparing the black, blue and green lines, it can be seen that the density peak initially occurs near the LCFS, then goes outward into the scrape-off layer. Later on, the fragments ultimately penetrate deeper into the plasma and result in core density rise in the late injection phase, as shown by the cyan and red lines. Note that the density rise in the axis region represented by the red line Fig. 2(a) is due

Case #	Assim. Ne	Assim. H	f_{rad}	t_{TQ} (90%-20%)	Max. ΔQ
BH-FP-dt0	9.91×10^{21}	6.40×10^{23}	49.4%	2.0ms	$25.4 MWs^{1/2}/m^2$
DH-FP-dt0	$\sim 1.1 \times 10^{22}$	$\sim 8.00 \times 10^{23}$	$\sim 76.5\%$	$\sim 3.1ms$	$16MWs^{1/2}/m^2$
DH-QP-dt0	2.53×10^{22}	4.40×10^{23}	89.8%	4.4ms	$5.7 MW s^{1/2}/m^2$
DH-QP-dt1	2.15×10^{22}	3.58×10^{23}	86.3%	4.2ms	$14.9 MW s^{1/2}/m^2$
DH-QP-dt0-ff	2.82×10^{22}	5.54×10^{23}	81.3%	2.4ms	$16.6 MW s^{1/2}/m^2$
DH-QP-dt0-120	$\sim 2.5 \times 10^{22}$	$\sim 4.40 \times 10^{23}$	$\sim 84.5\%$	$\sim 4.4ms$	$11.6MWs^{1/2}/m^2$
DH-QP-stg	9.64×10^{21}	8.92×10^{23}	78.4%	7.91ms	$5.9 MWs^{1/2}/m^2$

Table 2 – The neon and hydrogen assimilation, radiated fraction, TQ time and maximum local energy impact for seven cases considered in this section. The tilde signs indicate the estimated result extrapolated from the half-finished simulation result.

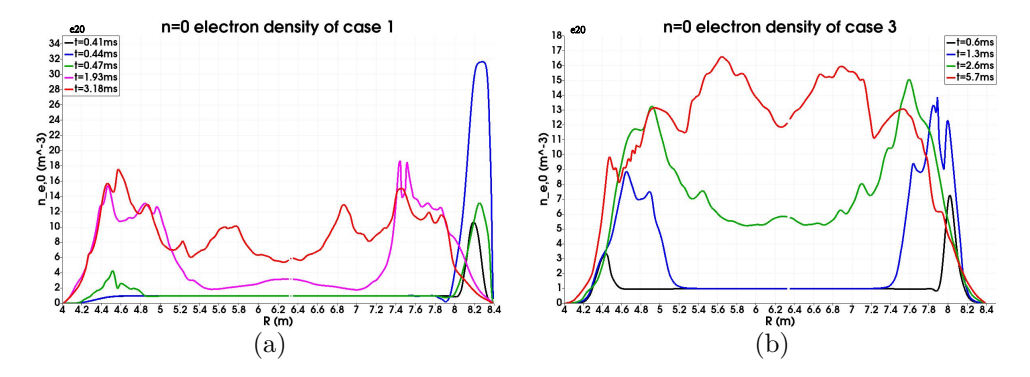


Figure 2 – The mid-plane cut of the n=0 electron density for (a) BH-FP-dt0 and (b) DH-QP-dt0 at various times. The high pedestal temperature and the consequential plasmoid drift in BH-FP-dt0 results in significant density deposition outside of the pedestal in the early injection phase as is shown by the black, blue and green lines in (a). The LCFS on the low field side approximately locates at R=8.2m. Taken from Ref. [23]

to inward MHD transport, as at the corresponding time the majority of fragments has not reached the axis yet. This behaviour is compared with DH-QP-dt0 shown in Fig. 2(b), where no apparent density expulsion is seen and the density peak gradually moves inward. The density rise shown by the green line in Fig. 2(b) is also due to the previously mentioned MHD mixing, while the later further density rise shown in the red line in Fig. 2(b) could be partly because the fragments reach the axis region and deposit material there.

One thing of note is that although the delay between injectors indeed negatively impacts the total assimilation, the effect is not drastic for a 1ms delay, as can be seen comparing DH-QP-dt1 with the other cases in Table 2. As is shown in Fig. 3 (a), the second plume, despite only facing an already significantly cooled down plasma, could still contribute up to 1/3 of the total assimilation by the end of the simulation. This is consistent with the fact that the electron density profile of DH-QP-dt1 is only slightly lower compared with the other cases, as is shown in Fig. 3 (b), where the flux averaged electron density profiles of all cases are compared.

Another feature to be noted in Fig. 3 (b) is that the staggered case DH-QP-stg shows significantly higher

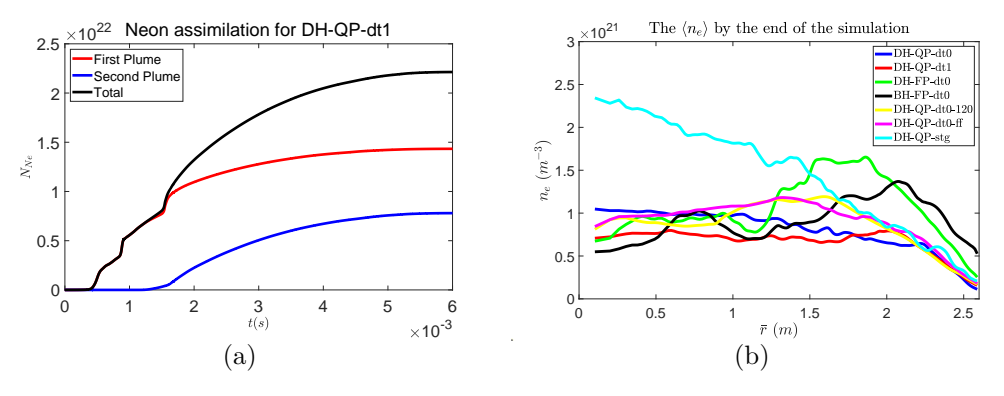


Figure 3 – (a) The asymmetry in the plume assimilation for the DH-QP-dt1 case; (b) The flux averaged electron density profile at the end of the simulation for each of the cases.

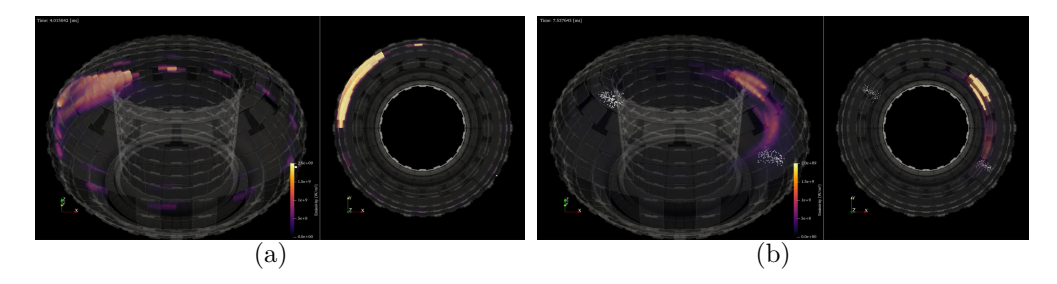


Figure 4 – The radiation power density within the plasma at time (a) t = 0.8ms and (b) t = 4.3ms after the first plume fragment arrival for DH-QP-dt1 case. The white spots represent the fragment position, including those fragments that are already fully ablated.

density rise near the magnetic axis, despite similar level of total assimilation compared with the non-staggered full pellet case DH-FP-dt0. This probably is due to the ablation occurring deeper into the core for the following neon-mixed plumes, as the edge is diluted by the H plumes without triggering the TQ. The staggered case also shows remarkably weaker MHD response in the early neon-mixed pellet injection phase compared with the other cases, due to its weaker ablation in the already-cooled-down plasma edge. Whether this behaviour is retained in an intrinsic neon seeded plasma remains part of future investigations.

3.2. The radiation asymmetry

The assessment of radiation asymmetry is obtained both within the plasma, and most importantly, on the first wall. As mentioned above, the JOREK radiation power density is projected onto the realistic ITER first wall tiles via the IMAS integrated RaySect/CHERAB code suite, the radiation heat fluxes thus obtained are then used to calculate the energy impact as described in Section 2. Note that in this work we assume the plasma to be always transparent, which might overestimate the radiation heat flux. Thus the results presented here should be considered as an upper estimation.

An example of the radiation power density distribution for DH-QP-dt1 case [31] is shown in Fig. 4. In this asymmetric injection case, the radiation band is first seen concentrate around the first plume (upper left corner) at t = 0.8ms as is shown in Fig. 4(a), while later on the radiation band is seen to stem from the second plume (lower right corner) at t = 4.3ms. This shows that despite the injection asymmetry, the second plume still contributes to the radiative depletion of the thermal energy.

Projecting the above radiation power density onto the first wall, one could calculate the consequential energy impact as is shown in Fig. 5. Here, Fig. 5(a), (b) and (c) are looking at the EQ-08 port at time 0.56ms, 0.94ms and 5.74ms respectively, while Fig. 5(d) is looking at the EQ-17 port at time 5.74ms. Evident radiation asymmetry around the port region can be seen in Fig. 5(a) and (b), while it gradually relaxes as the TQ proceed, as can be seen by comparing Fig. 5(c) and (d) to Fig. 5(a) and (b). This feature of strong radiation asymmetry in the early injection phase and relaxed asymmetry in the late TQ phase has been reported in Ref. [23] previously.

Despite the initial strong radiation asymmetry close to the injection port, none of the cases concerned in our study show maximum energy impact above the tungsten melting threshold at $38MWs^{1/2}/m^2$ [11], as can be seen in Table 2. The highest energy impact occurs in those cases with strong asymmetry in either the injection configuration itself (BH-FP-dt0 and DH-QP-dt1, for example) or in the MHD response (DH-FP-dt0 and DH-QP-dt0-ff, for example). For the latter cases, despite a symmetric SPI setup, the MHD response shows odd parity components when it grows to strong enough amplitude, resulting in an asymmetry in the outgoing heat flux, and thus in the ensuing ablation and radiation. For the SS, the maximum energy impact near the injection port would exceed its melting threshold at $13MWs^{1/2}/m^2$ [14]. However, past experiments have confirmed that exposure to such level of heat flux would only result in surface roughening of SS but no significant loss of material [13].

Another interesting observation is that stronger radiation asymmetry within the plasma would not necessarily translate into stronger energy impact on the first wall, as is shown in Fig. 6. Here, the red solid line represents the DH-QP-stg case and the blue one represents the DH-QP-dt0 case. The horizontal axis is the Toroidal Peaking Factor (TPF), calculated by taking the maximum integrated radiation power across all simulation poloidal planes, then dividing this maximum value by the averaged radiation power across all poloidal planes. The vertical axis corresponds to the total radiation power. The lines show the trajectory of both cases in the TPF- P_{rad} plane over time. It can be seen that the DH-QP-stg consistently shows stronger TPF compared with the DH-QP-dt0 case, which is due to the slower relaxation of the impurity density around the fragments in a colder plasma already cooled down by the preceeding H plume. Such higher radiation power density asymmetry within the plasma,

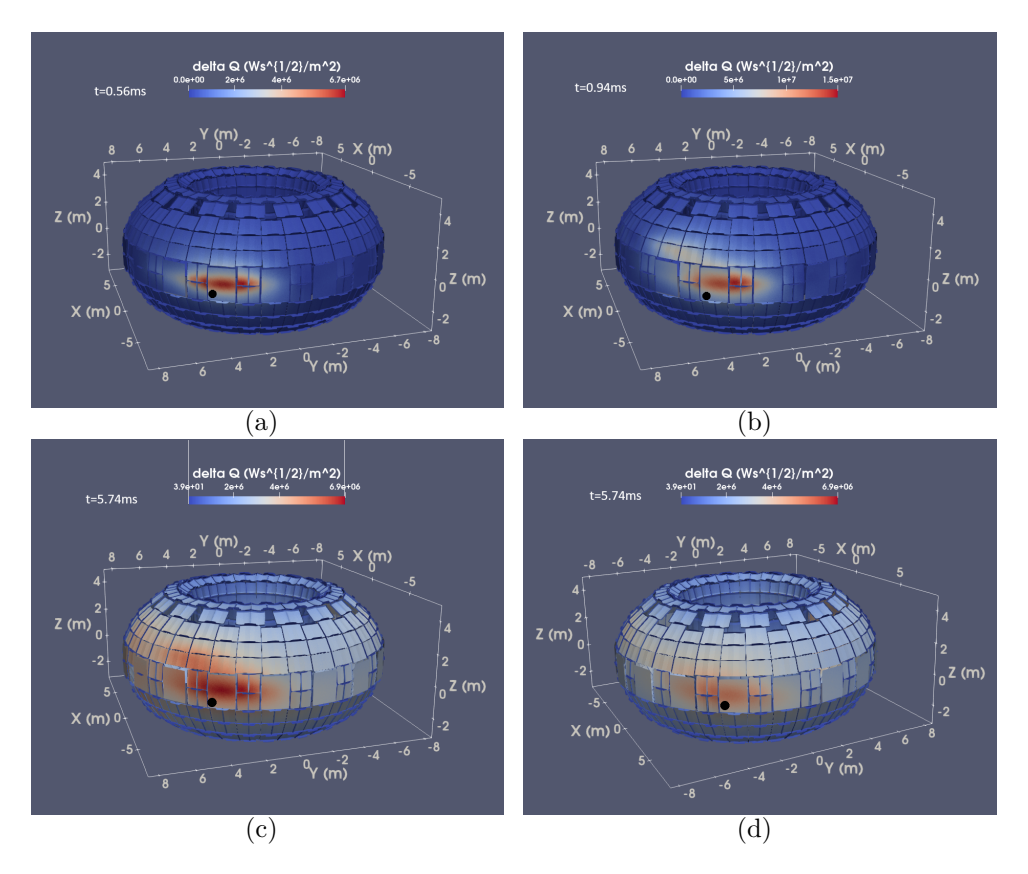


Figure 5 – The first wall energy impact of DH-QP-dt1 calculated using Eq. 1 at (a) t = 0.56ms looking at port EQ-08, (b) t = 0.94ms looking at port EQ-08, (c) t = 5.74ms looking at port EQ-08 and (d) t = 5.74ms looking at port EQ-17. The EQ-08 and EQ-17 ports are marked by the black dots. Taken from Ref. [23].

however, does not translate into higher energy impact asymmetry onto the first wall, as can be seen by comparing the DH-QP-stg and DH-QP-dt0 row in Table 2. This is because the neon deposition is deeper for DH-QP-stg compared with DH-QP-dt0, hence the radiation occurs further away from the first wall. Thus the geometry effect mitigates the stronger radiation power density asymmetry.

4. CONCLUSION

Collisional-radiative JOREK simulations of dual-SPI into ITER H-mode cases are carried out to investigate the characteristic assimilation and radiation asymmetry. It is found that strong plasmoid drift could occur when injecting the full pellet into an ITER baseline H-mode, resulting in premature thermal energy loss and material expulsion, detrimental to the mitigation. Considering a higher mixture ratio plume and the precursor confinment degradation suppress such effect. The delay between the dual injectors is found to reduce the total assimilation as would be expected, but its overall impact is found to be not very significant for a 1ms delay. The staggered injection scheme is found to result in significantly better core density penetration.

The radiation heat flux and its accumulated energy impact onto the first wall are obtained by ray-tracing from the volumetric radiation power density distribution provided by JOREK concerning seven different cases. It is found that the radiation heat deposition tends to concentrate around the injecting port in the early injection phase, while it spreads over larger areas towards the end of the TQ. With the quarter pellet, degraded H-mode and 1ms injection delay, the maximum radiation energy impact approaches the tolerable limit of the stainless steel plate while staying far below the tungsten limit. Good synchronization is found to further relax the energy impact distribution and reduce its maximum value, such that it never reaches the stainless steel limit for the perfect synchronized degraded H-mode case. These results are reassuring since they suggest the degraded H-mode with quarter pellet case could achieve high radiation fraction without the risk of melting the first wall. In the baseline H-mode case, despite the strong radiation power, its energy impact still stays well below the tungsten limit, although it exceeds that of the stainless steel substantially, hence one would expect melting of the diagnostic window armour plates. However, even if such melting occurs, it would not impede continued operation of ITER, as it has been found in previous studies with $22MWs^{1/2}/m^2$ heat pulses that the transient surface

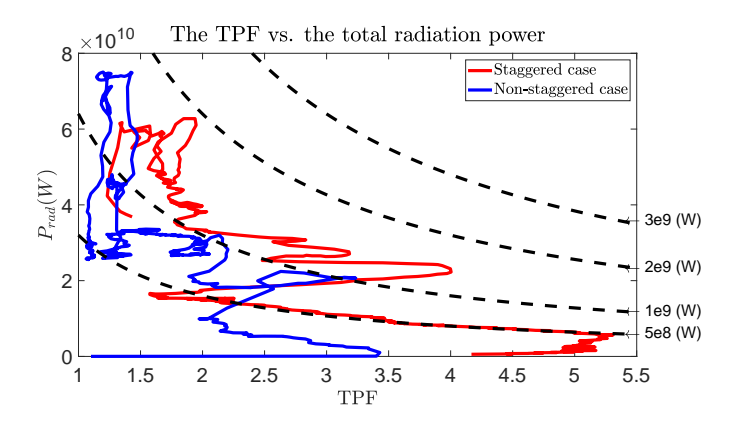


Figure 6 – The radiation TPF vs. the total radiation power for case DH-QP-dt0 and DH-QP-stg. The black dashed lines represents different levels of maximum integrated radiation power within each of the 64 poloidal planes used in the simulation.

melting would result in a surface roughening increasing at a rate of 1-2 micrometers per pulse, but no loss of material [13]. Another interesting observation is that the maximum energy impact is approaching the melting limit of the beryllium at $28MWs^{1/2}/m^2$ [14], so that the new ITER tungsten tiles provide more margin against radiation heat deposition compared with previous beryllium ones.

Overall, the study reported above serves as a first look into the radiation heat deposition on the ITER first wall during its H-mode TQ mitigation process using non-linear 3D simulation, which is part of ongoing validation work for the ITER PFC heat load specification. This study also provides input for more detailed first wall heat transport and material damage studies in the future.

ACKNOWLEDGEMENT

The authors thank S. Jachmich and A. Matsuyama for fruitful discussion. ITER is the Nuclear Facility INB no. 174. The views and opinions expressed herein do not necessarily reflect those of the ITER Organization. This publication is provided for scientific purposes only. Its contents should not be considered as commitments from the ITER Organization as a nuclear operator in the frame of the licensing process. Part of this work is supported by the National MCF Energy R&D Program of China under Grant No. 2019YFE03010001. This work has been co-funded by the ITER Organization under the implementing agreement IO/IA/19/4300002053. This work was supported in part by the Swiss National Science Foundation. Part of this work has been carried out within the framework of the EUROfusion Consortium, funded by the European Union via the Euratom Research and Training Programme (Grant Agreement No. 101052200 - EUROfusion). The Swiss contribution to this work has been funded by the Swiss State Secretariat for Education, Research and Innovation (SERI). Views and opinions expressed are however those of the author(s) only and do not necessarily reflect those of the European Union, the European Commission or SERI. Neither the European Union nor the European Commission nor SERI can be held responsible for them. This work is carried out partly on Tianhe-3 operated by NSCC-TJ and partly on the ITER cluster.

REFERENCES

- [1] M. Lehnen, K. Aleynikova, P.B. Aleynikov et al., "Disruptions in ITER and strategies for their control and mitigation" J. Nucl. Mater., 463, 39-48 (2015).
- [2] Y. Li, Z.Y. Chen, W. Yan et al., "Comparison of disruption mitigation from shattered pellet injection with massive gas injection on J-TEXT", Nucl. Fusion 61 126025 (2020).
- [3] U.A. Sheikh, D. Shiraki, R. Sweeney et al., "Disruption thermal load mitigation with shattered pellet injection on the Joint European Torus (JET)", Nucl. Fusion 61 126043 (2021).
- [4] S. Jachmich, U. Kruezi, M. Lehnen et al., "Shattered pellet injection experiments at JET in support of the ITER disruption mitigation system design", Nucl. Fusion 62 026012 (2022).
- [5] Juhyeok Jang, Jayhyun Kim, Jaewook Kim et al., "Radiation distribution for shattered pellet injection experiment with AXUV array diagnostics in KSTAR", Fusion Eng. Des. 180 113172 (2022).
- [6] B. Stein-Lubrano, R. Sweeney, D. Bonfiglio et al., "3D Radiated Power Analysis of JET SPI Discharges Using the Emis3D Forward Modeling Tool", Nucl. Fusion 64 036020 (2024).

- [7] C. C. Kim, Y. Liu, P. B. Parks et al., "Shattered pellet injection simulations with NIMROD" Phys. Plasmas, 26, 042510 (2019).
- [8] D. Hu, E. Nardon, M. Hoelzl et al., "Radiation asymmetry and MHD destabilization during the thermal quench after impurity Shattered Pellet Injection" Nucl. Fusion, 61, 026015 (2021).
- [9] D. Hu, E. Nardon, F.J. Artola et al., "Collisional-radiative simulation of impurity assimilation, radiative collapse and MHD dynamics after ITER Shattered Pellet Injection" Nucl. Fusion, 63, 066008 (2023).
- [10] J. McClenaghan, B.C Lyons, C.C. Kim et al., "MHD modeling of shattered pellet injection in JET" Nucl. Fusion, 63, 066029 (2023).
- [11] A. Herrmann, "Overview on stationary and transient divertor heat loads" Plasma Phys. Control. Fusion 44 (2002) 883–903.
- [12] Pietro Barabaschi, "Progress on manufacturing, construction, commissioning and an updated baseline", 29th Fusion Energy Conference, 16–21 Oct 2023, 2023, London, UK.
- [13] N.S. Klimov, J. Linke, R.A. Pitts et al., "Stainless steel performance under ITER-relevant mitigated disruption photonic heat loads", J. Nucl. Mater., 438, S241-S245 (2013);
- [14] R.A. Pitts, B. Bazylev, J. Linke et al., "Final case for a stainless steel diagnostic first wall on ITER" J. Nucl. Mater. 463 (2015) 748–752.
- [15] J W Coenen, V Philipps, S Brezinsek et al., "Analysis of structural changes and high-heat-flux tests on pre-damaged tungsten from tokamak melt experiments" Phys. Scr. T145 (2011) 014066.
- [16] G.G. van Eden, T.W. Morgan, H.J. van der Meiden et al., "The effect of high-flux H plasma exposure with simultaneous transient heat loads on tungsten surface damage and power handling" Nucl. Fusion 54 (2014) 123010.
- [17] Y. Yuan, J. Du, M. Wirtz et al., "Surface damage and structure evolution of recrystallized tungsten exposed to ELM-like transient loads" Nucl. Fusion 56 (2016) 036021.
- [18] Jun Wang, Chun Li, Yue Yuan et al., "Surface modification of W-V alloy exposed to high heat flux helium neutral beams" Nucl. Fusion 58 (2018) 096001.
- [19] Yue Yuan, Wangguo Guo, Peng Wang et al., "Influence of surface melting on the deuterium retention in pure and lanthanum oxide doped tungsten" Nucl. Fusion 59 (2019) 016022.
- [20] M. Hoelzl, G.T.A. Huijsmans, S. Pamela et al., "The JOREK non-linear extended MHD code and applications to large-scale instabilities and their control in magnetically confined fusion plasmas" Nucl. Fusion 61 065001 (2021).
- [21] M. Hoelzl, G.T.A. Huijsmans, F.J. Artola et al., "Non-linear MHD modelling of transients in tokamaks: a review of recent advances with the JOREK code" Nucl. Fusion 64 112016 (2024).
- [22] D Hu, G T A Huijsmans, E Nardon et al., "Collisional-radiative non-equilibrium impurity treatment for JOREK simulations" Plasma Phys. Control. Fusion 63 125003 (2021).
- [23] D. Hu, F.J. Artola, E. Nardon et al., "Plasmoid drift and first wall heat deposition during ITER H-mode dual-SPIs in JOREK simulations" Nucl. Fusion, 64, 086005 (2024).
- [24] S.H. Kim, T.A. Casper and J.A. Snipes, "Investigation of key parameters for the development of reliable ITER baseline operation scenarios using CORSICA", Nucl. Fusion 58 056013 (2018);
- [25] V. Riccardo, A. Loarte and the JET EFDA Contributors, "Timescale and magnitude of plasma thermal energy loss before and during disruptions in JET", Nucl. Fusion 45 1427 (2005);
- [26] P. B. Parks, "Modeling dynamics Fracture of Cryogenic Pellets", GA report GA-A28352, (2016).
- [27] T.E. Gebhart, L.R. Baylor & S.J. Meitner, "Shatter Thresholds and Fragment Size Distributions of Deuterium-Neon Mixture Cryogenic Pellets for Tokamak Thermal Mitigation", Fusion Sci. Technol., 76:7 831-835 (2020).
- [28] T. E. Gebhart, L. R. Baylor, and S. J. Meitner, "Analysis of the Shattered Pellet Injection Fragment Plumes Generated by Machine Specific Shatter Tube Designs", Fusion Sci. Technol., 77:1, 33-41 (2021);
- [29] M. Carr et al., Raysect Python Raytracing Package (v0.4.0). Zenodo. https://doi.org/10.5281/zenodo.1205064.
- [30] M. Carr et al., cherab/core: Zenodo. https://doi.org/10.5281/zenodo.3551871
- [31] K. Munechika, et al., "Synthetic framework for ITER bolometer performance assessment", o26, 6th European Conference on Plasma Diagnostics, Prague, Czechia, 2025